Origin of emission from square-shaped organic microlasers

2016 EPL 113 54002

(http://iopscience.iop.org/0295-5075/113/5/54002)

A LETTERS JOURNAL EXPLORING THE FRONTIERS OF PHYSICS

March 2016

EPL, **113** (2016) 54002
doi: 10.1209/0295-5075/113/54002

www.epljournal.org

Origin of emission from square-shaped organic microlasers

S. BITTNER[1,2], C. LAFARGUE[1], I. GOZHYK[1,3], N. DJELLALI[1], L. MILLIET[1], D. T. HICKOX-YOUNG[1], C. ULYSSE[4], D. BOUCHE[5], R. DUBERTRAND[6], E. BOGOMOLNY[7], J. ZYSS[1] and M. LEBENTAL[1(a)]

[1] *Laboratoire de Photonique Quantique et Moléculaire, ENS Cachan, Centrale Supélec, CNRS, Université Paris-Saclay - F-94235 Cachan, France*
[2] *Department of Applied Physics, Yale University - New Haven, CT 06520, USA*
[3] *Surface du Verre et Interfaces, UMR 125 CNRS/Saint-Gobain Recherche - 39 quai Lucien Lefranc, F-93303 Aubervilliers, France*
[4] *Laboratoire de Photonique et Nanostructures, CNRS UPR20 - Route de Nozay, F-91460 Marcoussis, France*
[5] *Centre de Mathématiques et de leurs Applications, ENS Cachan, CNRS, Université Paris-Saclay F-94235 Cachan, France*
[6] *Département de Physique, Université de Liège - 4000 Liège, Belgium*
[7] *Université Paris-Sud, Laboratoire de Physique Théorique et Modèles Statistiques, CNRS UMR 8626 Orsay, F-91405, France*

received 22 January 2016; accepted in final form 15 March 2016
published online 31 March 2016

PACS 42.55.Sa – Microcavity and microdisk lasers
PACS 03.65.Sq – Semiclassical theories and applications
PACS 05.45.Mt – Quantum chaos; semiclassical methods

Abstract – The emission from open cavities with non-integrable features remains a challenging problem of practical as well as fundamental relevance. Square-shaped dielectric microcavities provide a favorable case study with generic implications for other polygonal resonators. We report on a joint experimental and theoretical study of square-shaped organic microlasers exhibiting a far-field emission that is strongly concentrated in the directions parallel to the side walls of the cavity. A semiclassical model for the far-field distributions is developed that is in agreement with even fine features of the experimental findings. Comparison of the model calculations with the experimental data allows the precise identification of the lasing modes and their emission mechanisms, providing strong support for a physically intuitive ray-dynamical interpretation. Special attention is paid to the role of diffraction and the finite side length.

Introduction. – Semiclassical physics emerged during the development of quantum mechanics, almost one century ago, to account for the transition from wave physics in the quantum regime to classical mechanics [1]. Today, semiclassical physics plays an essential role in quantum chaos [2], and its methods are applied in virtually any field that features wave dynamics, including acoustics [3], electromagnetism [2], hydrodynamics [4], and loop quantum gravity [5]. We demonstrate the power of these methods when applied to optical microresonators by studying square-shaped polymer-based microlasers. Their emission properties are little understood for two reasons. Firstly, the square resonator with Dirichlet boundary conditions is a standard example of a separable system, whereas the dielectric square resonator is nonseparable and hence nonintegrable due to the diffraction at the dielectric corners. This remains an open problem in mathematical physics with tremendous impact on radar or telecommunication applications [6]. Secondly, it was observed that these lasers emit very narrow lobes in only a few directions. Directional emission from microlasers has been intensely investigated due to possible applications [7] and observed for, *e.g.*, Limaçon- and stadium-shaped microlasers. The underlying mechanism is understood in terms of their chaotic ray dynamics [8,9]. However, these explanations cannot be applied to polygonal resonators since they do not exhibit chaotic ray dynamics.

While square and hexagonal microresonators and -lasers have been extensively studied, their far-field distributions have been scarcely investigated [10–13]. This is partly because rounded corners significantly influence the resonance frequencies and field distributions [10,14–16], and

(a) E-mail: lebental@lpqm.ens-cachan.fr

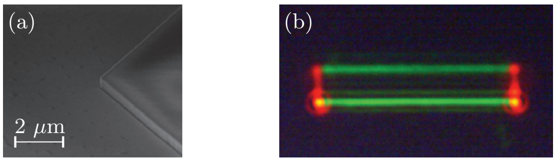

Fig. 1: (Color online) (a) Scanning electron microscope image of a square microlaser. (b) Perspective photograph in real colors of a lasing square cavity with side length 120 μm. The side walls parallel to the camera axis emit red laser light, whereas the side walls perpendicular to it scatter the green pump laser.

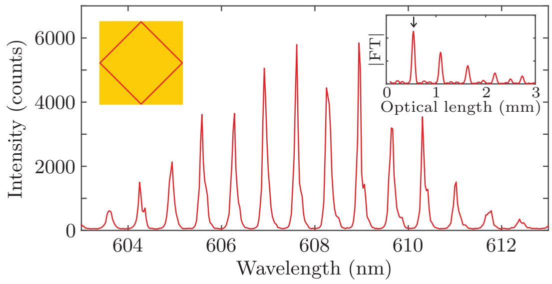

Fig. 2: (Color online) Experimental spectrum of a square microlaser with 120 μm side length at $\varphi = 0°$ at about 2.5 times the threshold intensity ($I_{\mathrm{thres}} = 2.5\,\mathrm{MW\,cm^{-2}}$) and with linearly polarized pump beam. The left inset shows the diamond periodic orbit in the square billiard. The right inset shows its Fourier transform. The arrow indicates the optical length of the diamond orbit.

it is technologically challenging to fabricate sharp corners. Here we investigate the far-field emission of microlasers with sharp corners (*i.e.*, with a radius of curvature much smaller than the wavelength). A semiclassical model for the dielectric square [17,18] is used to predict the far-field distributions, which are in very good agreement with numerical calculations. Careful comparison of the measured far-field distributions with the model allows to identify the lasing modes and understand the mechanism for their high directionality.

Experiments. – The microlasers consisted of a PMMA[1] polymer matrix doped by 5 wt% DCM[2] laser dye that was deposited in a 650 nm thick layer on a Si/SiO_2 (2 μm) wafer by spin-coating. Square cavities with side length ranging from $a = 80$ to 200 μm were engraved by electron-beam lithography [19], which makes it possible to obtain two-dimensional cavities with nanoscale precision (see fig. 1(a)).

The microlasers were pumped by a pulsed, frequency-doubled Nd:YAG laser (532 nm, 0.5 ns, 10 Hz). The short pulses and low duty cycle help to avoid problems from heating and quenching due to dark states. The pump beam impinged vertically and it covered the whole cavity uniformly. The lasing emission was collected in the sample plane by a lens and transferred to a spectrometer by an optical fiber. It was polarized parallel to the sample plane. The far-field intensity distributions were measured as a function of the azimuthal angle φ by rotating the cavity.

A typical spectrum is shown in fig. 2. It features a sequence of equidistant peaks. Its Fourier transform (right inset of fig. 2) shows that the free spectral range (FSR) of the spectrum corresponds to the optical length of the diamond orbit [20,21]. Therefore, it is expected that the observed lasing modes are localized on trajectories with an angle of incidence close to 45°.

A typical far-field intensity distribution of a single resonance is presented in fig. 3(a). It exhibits four emission lobes in the directions parallel to the side walls. The emission lobes are very narrow with a full width at half-maximum of about 6° (see fig. 3(b)). Figure 1(b) shows an image of the lasing cavity taken by a camera

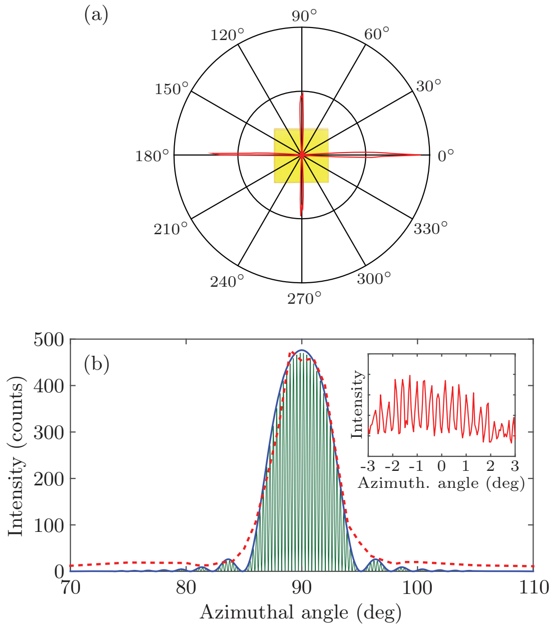

Fig. 3: (Color online) (a) Measured far-field intensity distribution of a single resonance at $\lambda = 606.7$ nm for circularly polarized pump beam. The photograph of the cavity indicates its orientation. (b) Magnification around the lobe at 90°. The dashed red line is the measured intensity distribution, the solid blue line the fitted intensity envelope, and the thin green line the corresponding calculated intensity distribution. The inset shows a measurement with higher angular resolution and linearly polarized pump around 0°.

with a high-magnification zoom lens. It evidences that the lasing emission (red) is emitted from the side walls parallel to the emission direction, whereas the side walls perpendicular to it do not emit but only scatter the green pump laser. Since the emission is at a grazing angle, it must stem from rays impinging on the cavity side walls with an angle of incidence very close to the critical one, $\alpha_{\mathrm{crit}} = \arcsin(1/n) = 41.8°$, where $n = 1.5$ is the refractive index [20]. This is in agreement with the previous

[1]Poly(methyl methacrylate) PMMA A6 resist by Microchem.
[2]4-(Dicyanomethylene)-2-methyl-6-(4-dimethylaminostyryl)-4Hpyran by Exciton.

Table 1: Symmetry classes, quantum numbers and model WFs (adapted from ref. [18]).

Diagonal symmetry	Horizontal/vertical symmetry	Parity of $m_x + m_y$	Parity of $m_x \cdot m_y$	Mulliken symbol	Model wave function
$(++)$	$+$	Even	Even	A_1	$\Psi_{\text{mod}}(x,y) = \Psi_0[\cos(k_x x)\cos(k_y y) + \cos(k_y x)\cos(k_x y)]$
$(--)$	$+$	Even	Even	B_2	$\Psi_{\text{mod}}(x,y) = \Psi_0[\cos(k_x x)\cos(k_y y) - \cos(k_y x)\cos(k_x y)]$
$(++)$	$-$	Even	Odd	B_1	$\Psi_{\text{mod}}(x,y) = \Psi_0[\sin(k_x x)\sin(k_y y) + \sin(k_y x)\sin(k_x y)]$
$(--)$	$-$	Even	Odd	A_2	$\Psi_{\text{mod}}(x,y) = \Psi_0[\sin(k_x x)\sin(k_y y) - \sin(k_y x)\sin(k_x y)]$
$(+-)$	None	Odd	Even	E	$\Psi_{\text{mod}}(x,y) = \Psi_0[\sin(k_x x)\cos(k_y y) + \cos(k_y x)\sin(k_x y)]$
$(-+)$	None	Odd	Even	E	$\Psi_{\text{mod}}(x,y) = \Psi_0[\sin(k_x x)\cos(k_y y) - \cos(k_y x)\sin(k_x y)]$

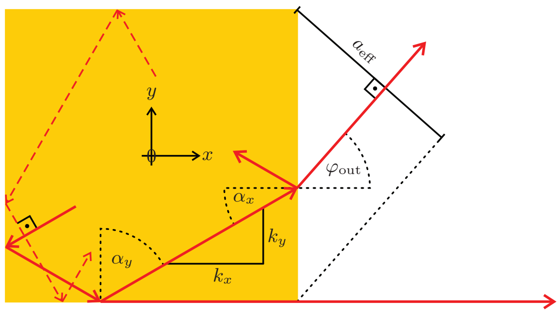

Fig. 4: (Color online) Sketch of rays with momentum vectors $\pm k_x\vec{e}_x \pm k_y\vec{e}_y$ (solid red lines). Their angles of incidence on the vertical (horizontal) side walls are α_x ($\alpha_y = \pi/2 - \alpha_x$). The angle of refraction is φ_{out}. The dashed red lines indicate rays with momentum vectors rotated by 90°, $\pm k_y\vec{e}_x \pm k_x\vec{e}_y$.

observation that the ray trajectories on which the lasing modes are based have an angle of incidence close to 45°.

Model calculations. – The far-field distributions are calculated using the semiclassical model introduced in refs. [17,18] to identify the observed lasing modes. The model is based on the observation that the wave functions are localized on classical tori and are thus composed of eight plane waves $\exp\{i(k_x x + k_y y)\}$. Their directions are related to each other by the symmetry operations of the C_{4v} point group. The corresponding ray trajectories in fig. 4 are given by the momentum vectors $\pm k_x\vec{e}_x \pm k_y\vec{e}_y$ and their rotations by 90°, $\pm k_y\vec{e}_x \pm k_x\vec{e}_y$.

To quantize the spectrum, the simplest approach is to separate the system along the x and y directions, and write two phase loop conditions analogous to that of a Fabry-Pérot cavity [17,18],

$$\begin{aligned} r^2(\alpha_x)\, e^{ik_x 2a} &= 1, \\ r^2(\alpha_y)\, e^{ik_y 2a} &= 1. \end{aligned} \tag{1}$$

The main difference from a Fabry-Pérot cavity are the Fresnel coefficients r corresponding to an incidence with angles $\alpha_{x,y} = \arctan[\text{Re}(k_{y,x})/\text{Re}(k_{x,y})]$ instead of 0°. The momentum vector components $k_{x,y}$ can thus be formally written as

$$\begin{aligned} k_x &= \{\pi m_x + i\ln[r(\alpha_x)]\}/a, \\ k_y &= \{\pi m_y + i\ln[r(\alpha_y)]\}/a. \end{aligned} \tag{2}$$

The resonance wave number is $k = 2\pi/\lambda = (k_x^2 + k_y^2)^{1/2}/n$, where λ is the free-space wavelength. Note that $k_{x,y}$ are in general complex-valued. All wave functions $\Psi(x,y)$ are obtained by adding up the 8 plane waves with their correct momentum vectors and signs. For transverse magnetic (TM) (transverse electric (TE)) polarization, the electric (magnetic) field is parallel to the plane of the cavity, and Ψ corresponds to the z component of the electric (magnetic) field. The resonances (*i.e.*, solutions of eq. (1)) are labeled by their quantum numbers $m_{x,y}$ and their symmetries s_1 (s_2) with respect to the diagonal $x = y$ ($x = -y$) as $(m_x, m_y, s_1 s_2)$, where $s_{1,2} = +1$ ($s_{1,2} = -1$) means a symmetric (antisymmetric) wave function. There are six symmetry classes corresponding to the different combinations of $s_{1,2}$ and the quantum numbers that are labeled by the Mulliken symbols $A_{1,2}$, $B_{1,2}$ and E (see table 1).

Green's identity is used to infer the far-field distribution [11]. The derivation is detailed in ref. [22] along with the comparison to numerical simulations. The full expression for the far-field distribution of an A_2 mode is given in eq. (S6) of ref. [22]. It consists of 8 terms like

$$\begin{aligned} &\text{sinc}\left\{(k_y - k\sin\varphi)\frac{a}{2}\right\}\left[\mu k_x \frac{a}{2}\cos\left(k_x\frac{a}{2}\right)\sin\left(k\frac{a}{2}\cos\varphi\right)\right. \\ &\left.- k\frac{a}{2}\cos\varphi\cos\left(k\frac{a}{2}\cos\varphi\right)\sin\left(k_x\frac{a}{2}\right)\right], \end{aligned} \tag{3}$$

where $\mu = 1$ ($\mu = 1/n^2$) for TM (TE) polarization and $\text{sinc}(x) = \sin(x)/x$. Each such term corresponds to emission in the two directions φ_{out} defined by the roots of the argument of the sinc function. If the angle of incidence of the corresponding rays inside the resonator is smaller than α_{crit}, then φ_{out} is simply given by Snell's law (see fig. 4), and the emission lobe is called *refractive*. Then the sinc term is in fact the diffraction pattern of a plane wave going through a slit with a width a_{eff} that is the projection of the side of the square on the emission direction

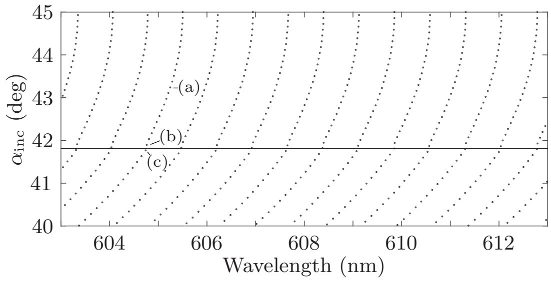

Fig. 5: Model calculation of the TE modes of a $a = 120\,\mu$m square with $n = 1.5$. The angle of incidence is plotted with respect to the resonance wavelength. The horizontal line indicates the critical angle. The model far-field intensity distributions of the modes marked (a), (b), and (c) are shown in fig. 6.

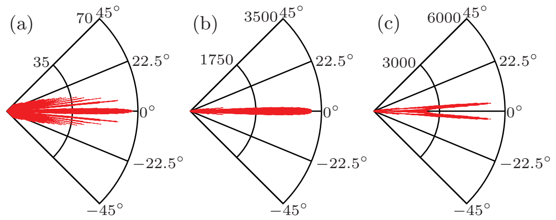

Fig. 6: (Color online) Model calculations of the far-field intensity distributions for a $a = 120\,\mu$m square with $n = 1.5$. The modes are (a) TE$(433, 407, --)$, (b) TE$(443, 397, --)$, and (c) TE$(444, 396, --)$.

(see fig. 4). When φ_{out} is complex, corresponding to rays with angle of incidence larger than α_{crit}, the lobe is called *nonrefractive* and is emitted parallel to the side wall. The nonrefractive lobes are jagged and much broader. They have a much smaller amplitude than the refractive lobes due to the finite imaginary part of φ_{out}. While no energy is transmitted when a plane wave impinges on an infinite dielectric interface with an angle larger than the critical one (*i.e.*, it is totally reflected), this is not the case for an interface of finite length as illustrated by the existence of the nonrefractive emission lobes [10], which leads to a modification of the reflection and transmission coefficients.

Two different cases of far-field diagrams can appear for $n = 1.5 > \sqrt{2}$, depending on $\alpha_{\mathrm{inc}} = \min\{\alpha_x, \alpha_y\}$. If $\alpha_{\mathrm{inc}} < \alpha_{\mathrm{crit}}$, the plane waves impinging on a side wall with angle α_{inc} escape refractively, whereas those impinging with $\pi/2 - \alpha_{\mathrm{inc}}$ are totally reflected. Hence 8 refractive and 8 nonrefractive lobes are observed, where the latter are typically negligible compared to the former. If $\alpha_{\mathrm{inc}} \geq \alpha_{\mathrm{crit}}$, all plane waves are totally reflected, and 16 nonrefractive lobes are observed, though their directions are fourfold degenerate.

Comparison with experiment. – We now compare the model with experiments. A spectrum generated by the model and corresponding to the experimental conditions is shown in fig. 5. The resonances are arranged in branches. Each of them consists of modes with identical longitudinal quantum number $m = m_x + m_y$ and increasing transverse quantum number $p = |m_x - m_y|/2$ as α_{inc} decreases [18]. The horizontal distance between these branches agrees well with the experimentally observed FSR, corresponding to the length of the diamond orbit. Therefore, we conclude that the observed lasing resonances belong to different branches, *i.e.*, each has a different m.

We use the far-field intensity distributions to infer α_{inc} and thus their transverse quantum numbers. The model far-field patterns of three representative modes are presented in fig. 6. They are labeled by (a), (b), and (c) in fig. 5. Mode (c) is located just below the critical angle ($p = 24$) and features two refractive emission lobes between $\varphi = -45°$ and $45°$, while its nonrefractive lobes are not visible due to their negligible amplitude. Since the measured far-field patterns feature only 4 lobes in the total range of 360°, such modes with $\alpha_{\mathrm{inc}} < \alpha_{\mathrm{crit}}$ can be excluded. Mode (b) with $p = 23$ is located just above the critical angle. The refractive lobes have become nonrefractive and merged into four narrow lobes parallel to the sides. This is precisely the kind of far-field pattern observed experimentally. Mode (a) finally is well above the critical angle ($p = 13$). The nonrefractive lobes have become very broad and jagged unlike what was observed experimentally. Also their amplitude has decreased significantly. This development continues with increasing α_{inc}. The qualitative comparison with the measured far-field intensity distribution shows that the experimental lasing modes are only consistent with mode (b), *i.e.*, an angle of incidence just above the critical angle. This is confirmed by the fits described in the following.

The experimental far-field distribution measured with an angular resolution of 1° as in fig. 3 is compared to the envelope of the model far-field distributions (see ref. [22] for details). The only two independent parameters are the amplitude and α_{inc}, which is considered a continuous variable due to the high resonance density. The fit of the lobe yields $\alpha_{\mathrm{inc}}^{(\mathrm{fit})} = 41.87°$ and is plotted in fig. 3(b). The agreement is excellent. Similar results are obtained for the other lobes and the other resonances as well as squares with various sizes, yielding values of $\alpha_{\mathrm{inc}}^{(\mathrm{fit})}$ from 41.81° to 41.96°. As expected from the qualitative considerations in the previous paragraph and the photograph in fig. 1(b), the angle of incidence is slightly above the critical angle.

In fact, the model predicts far-field distributions with a very quickly oscillating substructure that stems from the terms in the square brackets in eq. (3), namely the sin and cos functions with the argument $\phi = ka\cos(\varphi)/2$. The actual model far-field intensity distribution for the fitted parameters is shown as thin green line in fig. 3(b). To confirm this prediction, the angular resolution of the setup was improved by putting a slit in front of the collection lens. The far-field intensity distribution measured this way is shown in the inset of fig. 3(b). It features oscillations with a period of $(0.29 \pm 0.01)^\circ$, while the expected period is 0.29° according to eq. (3). The agreement is excellent for different wavelengths and cavity sizes.

Systematic measurements with increased angular resolution will allow for a better determination of the symmetry of the lasing resonances. Furthermore, the symmetry of the far-field distributions can be changed by the polarization of the pump laser due to the fluorescence anisotropy of the laser dye [23]: when the square microlaser is pumped with linear polarization parallel to the x-axis (instead of circular polarization as in fig. 3(a)), the emission is almost bidirectional with strong emission lobes at $\varphi = 0^\circ$ and 180°, whereas the emission lobes at 90° and 270° are strongly suppressed (not shown). This effect is a consequence of the lower degree of symmetry induced by the pump polarization. It can be explained by the formation of coherent superpositions of degenerate mode pairs like the A_1 and B_2 modes. It should be noted that the lasing modes and hence far-field emission of microlasers can also be controlled by localized or selective pumping [24–26], whereas controlling it only with the pump polarization is an experimentally simpler approach. These topics are, however, beyond the scope of this article and will be explored in a future publication.

Conclusions. – The far-field intensity distributions of square-shaped organic microlasers were investigated and revealed highly directional emission in the four directions parallel to the cavity sides. Sharp corners were essential for obtaining this high directionality because rounded corners significantly change the emission behavior [10]. Analytical formulas for the far-field distributions based on a semiclassical model [17,18] were developed and showed excellent agreement both with experimental data and with numerical simulations. They could be easily adapted to other polygonal cavities like hexagon or rectangles [11] and other refractive indices. The comparison between the model and experiments evidences that the lasing modes are based on trajectories with an angle of incidence almost equal to the critical angle that hence leave the resonator at a grazing angle. Interestingly, these modes do not feature the highest-quality factors; these would be modes with α_{inc} larger than α_{crit}. Maybe these modes actually lase, but are not observed because of their lower amplitude in the far-field compared to other modes. Or they may actually have higher losses due to diffraction at the substrate interface [19].

The semiclassical model does not take into account diffraction by the corners, whereas it is precisely this effect which renders the system nonintegrable. While the model calculations agree very well with the observed spectrum and far-field distributions, there are some minor observations that cannot be explained by them. For example, some light is emitted into other directions than the four main emission lobes due to diffraction at the corners, but it is much less intense[3]. This means that diffraction by the corner plays a secondary but not negligible role for the emission from polygonal microlasers. Studying these effects would allow more insight into the open physical-mathematical problem of diffraction by a dielectric wedge.

* * *

The numerical calculations are based on a code developed by C. Schmit. SB gratefully acknowledges funding from the European Union Seventh Framework Programme (FP7/2007-2013) under Grant No. 246.556.10. This work was supported by a public grant from the Laboratoire d'Excellence Physics Atom Light Matter (LabEx PALM) overseen by the French National Research Agency (ANR) as part of the Investissements d'Avenir program (Reference No. ANR-10-LABX-0039).

REFERENCES

[1] Brack M. and Bhaduri R. K., *Semiclassical Physics* (Westview Press, Oxford) 2003.
[2] Stöckmann H.-J., *Quantum Chaos: An Introduction* (Cambridge University Press, Cambridge, UK) 2000.
[3] Tanner G. and Søndergaard N., *J. Phys. A*, **40** (2007) R443.
[4] Kudrolli A., Abraham M. C. and Gollub J. P., *Phys. Rev. E*, **63** (2001) 026208.
[5] Bianchi E. and Haggard H. M., *Phys. Rev. Lett.*, **107** (2011) 011301.
[6] Gennarelli G., Frongillo M. and Riccio G., *IEEE Trans. Antennas Propag.*, **63** (2015) 374.
[7] Wiersig J., Unterhinninghofen J., Song Q., Cao H., Hentschel M. and Shinohara S., *Trends in Nano- and Micro-Cavities* (Bentham Science Publishers, Sharjah, United Arab Emirates) 2011, Chapt. 4, pp. 109–152.
[8] Schwefel H. G. L., Rex N. B., Tureci H. E., Chang R. K., Stone A. D., Ben-Messaoud T. and Zyss J., *J. Opt. Soc. Am. B*, **21** (2004) 923.
[9] Wiersig J. and Hentschel M., *Phys. Rev. Lett.*, **100** (2008) 033901.
[10] Wiersig J., *Phys. Rev. A*, **67** (2003) 023807.
[11] Yang Y.-D. and Huang Y.-Z., *IEEE J. Quantum Electron.*, **43** (2007) 497.
[12] Chen R. C. C., Yu Y. T., Huang Y. J., Chen C. C., Chen Y. F. and Huang K. F., *Opt. Lett.*, **34** (2009) 1810.
[13] Dai J., Xu C. X., Zheng K., Lv C. G. and Cui Y. P., *Appl. Phys. Lett.*, **95** (2009) 241110.
[14] Boriskina S. V., *IEEE J. Quantum Electron.*, **41** (2005) 857.
[15] Dietrich C. P., Lange M., Böntgen T. and Grundmann M., *Appl. Phys. Lett.*, **101** (2012) 141116.
[16] Kudo H., Suzuki R. and Tanabe T., *Phys. Rev. A*, **88** (2013) 023807.
[17] Bittner S., Bogomolny E., Dietz B., Miski-Oglu M. and Richter A., *Phys. Rev. E*, **88** (2013) 062906.

[3]See the Supplementary Material for a video of the rotating square microlaser: `RotatingSquareMicrolaser.avi`.

[18] Bittner S., Bogomolny E., Dietz B., Miski-Oglu M. and Richter A., *Phys. Rev. E*, **90** (2014) 052909.
[19] Lozenko S., Djellali N., Gozhyk I., Delezoide C., Lautru J., Ulysse C., Zyss J. and Lebental M., *J. Appl. Phys.*, **111** (2012) 103116.
[20] Lebental M., Djellali N., Arnaud C., Lauret J.-S., Zyss J., Dubertrand R., Schmit C. and Bogomolny E., *Phys. Rev. A*, **76** (2007) 023830.
[21] Bogomolny E., Djellali N., Dubertrand R., Gozhyk I., Lebental M., Schmit C., Ulysse C. and Zyss J., *Phys. Rev. E*, **83** (2011) 036208.
[22] Bittner S., Lafargue C., Gozhyk I., Djellali N., Milliet L., Hickox-Young D. T., Ulysse C., Bouche D., Dubertrand R., Bogomolny E., Zyss J. and Lebental M., arXiv:1601.07957 (2016).
[23] Gozhyk I., Clavier G., Méallet-Renault R., Dvorko M., Pansu R., Audibert J.-F., Brosseau A., Lafargue C., Tsvirkun V., Lozenko S., Forget S., Chénais S., Ulysse C., Zyss J. and Lebental M., *Phys. Rev. A*, **86** (2012) 043817.
[24] Ben-Messaoud T. and Zyss J., *Appl. Phys. Lett.*, **86** (2005) 241110.
[25] Bachelard N., Andreasen J., Gigan S. and Sebbah P., *Phys. Rev. Lett.*, **109** (2012) 033903.
[26] Liew S. F., Redding B., Ge L., Solomon G. S. and Cao H., *Appl. Phys. Lett.*, **104** (2014) 231108.